Advanced Powder Materials 4 (2025) 100276

Contents lists available at ScienceDirect

Advanced Powder Materials

journal homepage: www.keaipublishing.com/en/journals/advanced-powder-materials

Stereoisomeric engineering mediated zinc metal electrodeposition: Critical balance of solvation and adsorption capability

Wen Liu [a], Qiwen Zhao [a], Ruheng Jiang [a], Xuyan Ni [a], Tiancheng You [a], Canglong Li [c], Yanzi Deng [a], Bingang Xu [d], Yuejiao Chen [a,*], Libao Chen [a,b,**]

[a] State Key Laboratory of Powder Metallurgy, Central South University, Changsha 410083, China
[b] National Energy Metal Resources and New Materials Key Laboratory, Central South University, Changsha 410083, China
[c] School of Minerals Processing and Bioengineering, Central South University, Changsha 410083, China
[d] Nanotechnology Center, Research Institute for Intelligent Wearable Systems, The Hong Kong Polytechnic University, Hung Hom, Kowloon 999077, Hong Kong, China

ARTICLE INFO

Keywords:
Stereoisomeric additives
Structure-activity relationship
Coplanar templating effect
Solvation and adsorption capability
Optimized zinc deposition behavior

ABSTRACT

The exceptional electrochemical performance of zinc anodes is frequently impeded by inadequate deposition kinetics and interfacial chemistry. Herein, we introduce the stereoisomerism to inform the balanced selection of electrolyte additives, taking into account their solvation and adsorption properties, to achieve the optimal deposition behaviors and electrochemical performance. The three-point coplanar adsorption configuration, in comparison to two-point adsorption, effectively mitigates the interference of water molecules and establishes a coplanar templating effect. This approach fosters a uniform distribution of charges, encourages the preferential orientation growth of (002) planes for uniform zinc deposition. Moreover, an appropriate level of solvation ability can modulate the solvation structure without substantially increasing the de-solvation energy barrier, thereby facilitating faster deposition kinetics than what is observed in cases of strong solvation. As a result, Zn//Zn cell can achieve an excellent performance of more than 3470 h at 2 mA cm^{-2} and 1 mAh cm^{-2}, and Zn//AC full cell can work for 50000 cycles at 3 A g^{-1}. Additionally, under practical conditions (N/P=4.37), the assembled Zn//I_2 full cell demonstrates stable lifespan for 710 cycles at 1 A g^{-1}. This work showcases the interplay between adsorption configuration of stereoisomeric additives on the cycling.

1. Introduction

Although lithium-ion batteries occupy the vast market for new energy due to their excellent performance, thorny safety issues still have a certain impact on their position [1–6]. As a powerful alternative, aqueous zinc ion batteries (AZIBs) hold salient predominance in high safety, high reserves, and low cost [7–13]. However, metallic zinc (Zn) anode cannot well demonstrate its optimal performance [14–16]. Water is a significant factor contributing to corrosion and uneven deposition during the Zn plating/stripping process, both in the bulk electrolyte and at the interface between the electrolyte and electrode [17,18]. In the bulk electrolyte environment, H_2O molecules typically function as solvated water around cations or form a hydrogen bonding (H-bond) network by interacting with other surrounding H_2O molecules [19]. These behaviors will enhance the difficulty of cations de-solvation when plating and increase the possibility of hydrogen evolution [20–22]. Simultaneously, some free H_2O molecules will spontaneously adsorb onto the anode surface, reducing the corrosion resistance of the interface [23–25]. Even worse, these uneven absorbed H_2O will lead to ununiform Zn deposition, thus generating Zn dendrite and accelerating battery failure [26]. Therefore, reasonable control of H_2O molecules at the bulk and interface can effectively improve the stability of Zn anode and the cycling life of batteries.

To effectively manage water molecules at both the bulk electrolyte and interface, electrolyte additives are commonly incorporated into standard electrolytes [27–31]. Generally, these additives are designed to significantly reduce free H_2O molecules at the interface through adsorption effects or to sequester active H_2O within the bulk electrolyte by modulating the solvation structure of Zn^{2+} ions or disrupting the hydrogen-bond network [17,32,33]. Consequently, the solvation and

* Corresponding author.
** Corresponding author. State Key Laboratory of Powder Metallurgy, Central South University, Changsha 410083, China.
E-mail addresses: cyj.strive@csu.edu.cn (Y. Chen), lbchen@csu.edu.cn (L. Chen).
Peer review under the responsibility of Central South University.

https://doi.org/10.1016/j.apmate.2025.100276
Received 30 December 2024; Received in revised form 20 January 2025; Accepted 26 January 2025
Available online 6 February 2025

adsorption capabilities of additives are crucial criteria for evaluating their efficacy. The solvation strength of additives not only influences the formation of Zn^{2+} ion solvation structures in the bulk electrolyte but also affects the de-solvation of Zn^{2+} ions near the interface prior to deposition. Simultaneously, varying adsorption effects can create distinct electric double-layer (EDL) environments, thereby generating different deposition behaviors of Zn^{2+} ions. Additive molecules, predominantly organic compounds rich in functional groups, often exhibit isomerism, where compounds with the same molecular formula but different structures are referred to as structural isomers. These structural differences frequently result in divergent properties, and isomers have a broad spectrum of applications [34]. In this study, a pair of isomers was introduced to compare the solvation abilities and adsorption effects of additives on the Zn deposition behavior and the cycling stability of batteries.

Herein, sorbitol (Sor) and mannitol (Man), a pair of polyhydroxy stereoisomerisms, are chosen as electrolyte additives for designing two electrolyte systems to identify the equilibrium between solvation and adsorption. Both Sor and Man have six hydroxyl groups, with only the spatial position of the hydroxyl group on the second carbon being different (Fig. 1a). Furthermore, Sor is highly hygroscopic, while Man exhibits minimal hygroscopicity [35]. It is the structure-activity relationship between these two compounds that accounts for the observed differences in battery performance. Surprisingly, the trihydroxy group on the same side of Sor exhibits a stronger adsorption capacity than the dihydroxyl groups on the same side of Man. Moreover, adhering to the principle of determining a plane based on three points, it generates a coplanar templating effect. This effect promotes the uniform distribution of charges, increases nucleation sites, and induces (002) preferred growth. Compared to base $ZnSO_4$ electrolyte, Sor and Man molecules present stronger binding energy with Zn^{2+} ions and they can participate in solvation structure of Zn^{2+} ions. Due to the weaker interaction force between Sor molecular and Zn^{2+} ions compared to Man, it ensures a faster de-solvation process and accelerates the deposition kinetics. Meanwhile, in the bulk electrolyte, Sor molecules interact with H_2O, disrupting the original strong hydrogen-bond network. This significantly reduces the influence of free H_2O. These unique advantages make Zn anode in Sor added electrolyte demonstrate more exceptional performance for more than 3470 h at 2 mA cm^{-2} and 1 mAh cm^{-2}. Moreover, Zn//AC full cell with Sor additive can steadily operate for 50000 cycles at 3 A g^{-1}. In order to test the practical application, Zn//I_2 full cell under low N/P ratio of 4.37 can also steadily run for 710 cycles at 1 A g^{-1}, exhibiting superior lifespan than bare $ZnSO_4$ electrolyte.

2. Results and discussion

In an aqueous solution containing 2M $ZnSO_4$ (base electrolyte, denoted as BE), the solvation structure of Zn^{2+} ion is formed by the coordination of one Zn^{2+} ion with six H_2O molecules or five H_2O molecules and one SO_4^{2-}, as presented in Fig. 1b. Free H_2O molecules unevenly adsorb on the surface of Zn anode, which will trigger occurrence of hydrogen evolution reaction (HER) and corrosion. Seriously, owing to uneven adsorption of H_2O and defect on Zn foil surface, Zn^{2+} ions trend to accumulate at limited sites and cause local charge concentration, thus leading to two-dimension (2D) diffusion and Zn dendrite growth. When adding Man into $ZnSO_4$ electrolyte (marked as MAE), Man molecules can replace position of solvated H_2O surrounding Zn^{2+} ions. The dihydroxy group adsorption of Man blocks the most of H_2O near interface, hindering the occurrence of side reactions and promoting uniform Zn deposition. The electrolyte containing Sor (SAE) demonstrates more outstanding advantages. Sor molecules can also participate in the solvation structure of Zn^{2+}, but exhibit weaker binding energy with Zn^{2+} and form a moderate solvation shell to facilitate a faster de-solvation process. Sor provide stronger interaction with H_2O molecules in the electrolyte, thus breaking strong H-bond network. In addition, more stable adsorption of trihydroxy group ensures faster 3D diffusion and construct coplanar templating effect, inducing preferential oriented (002) deposition for dendrite-free growth.

Fig. S1 exhibits the solubility of BE with different concentrations of Man and Sor at room temperature. It can be clearly observed that 0.5 M–2 M SAE are all clarified solutions, while there are obvious precipitates in 2 M MAE. The solubility of Sor is much higher than that of Man at room temperature [36]. Spectral tests were performed to compare the macroscopic properties of these electrolytes. Nuclear magnetic resonance (^2H NMR) measurements were firstly conducted to investigate interaction between additives and H_2O molecule, as exhibited in Fig. 1c and S2. The chemical shift of ^2H in pure D_2O is located at 4.702 ppm (Fig. S2), and an obvious shift to 4.71 ppm after adding 2 M $ZnSO_4$, which is owing to the form of $(Zn(D_2O)_6)^{2+}$ [37]. Upon the introduction of Sor, the chemical shift of ^2H continues to undergo a blue shift as the amount of Sor increases. This indicates a decrease in the electron density of D_2O and the emergence of interaction between Sor and D_2O [38]. On the contrary, ^2H NMR moves to high field after adding different concentrations of Man to 2 M $ZnSO_4$, manifesting that there is no significant interaction between Man and H_2O molecules. It also indirectly explains the interaction between the additive and Zn^{2+} ions [39,40]. Fourier transform infrared spectroscopy (FTIR) tests were further performed to characterize additives influence. Fig. 1d and S3 are FTIR spectra of BE, MAE and SAE, in which the concertation of Man and Sor is 0.5 M. The v-SO_4^{2-} vibration (located from 1000 to 1200 cm^{-1}) both in MAE and SAE present red shift owing to weakened interaction between Zn^{2+} ions and SO_4^{2-}, implying the adjustment of Zn^{2+} ions solvation structure (Fig. 1d). The broadband ranges from 1560 to 1680 cm^{-1} and 3000 to 3800 cm^{-1} are corresponding to O-H vibration of water. As displayed in Fig. S3b-c, a blue shift can be observed in SAE compared to BE, which illustrates the weaken of H-bond between H_2O molecules attributing to the interaction between Sor and H_2O molecules. While, MAE shows a slight red shift caused by an increase in the number of H-bond. The FTIR spectra of SAE with different concertation Sor (0.2 M–1 M) are displayed in Fig. 1e–f and S4. As the increase of Sor, the red shift of v-SO_4^{2-} vibration and blue shift of O-H all indicate the weaken of Zn^{2+} ions and SO_4^{2-}, as well as H-bond network due to Sor. Furthermore, specific analysis of Raman spectra of O-H stretching vibration were conducted and the broadband ranges from 3000 to 3800 cm^{-1} can be divided into three kinds of H-bond, strong H-bond, medium H-bond and weak H-bond [41,42]. The strong H-bond ration is 44.2, 45.09 and 35.25 in BE, MAE and SAE, respectively (Fig. 1d and S5). The strong H-bond ratio in SAE is significantly lower than that in BE and MAE due to the interaction between Sor and H_2O molecules, which is well consistent with the above characterization. The slight increase in the proportion of strong H-bond of MAE is due to the fact that Man has almost no hygroscopicity, and its interaction with water molecules is weak. Moreover, Raman analysis was also conducted on electrolytes with different amounts of Sor (Fig. 1h and S6). With the addition of Sor, the strong H-bond ratio gradually decreases, which implying the function of Sor on breaking strong H-bond network. The contact angle (CA) between three electrolytes and Zn anode were further measured in Fig. 1i and S7. The CA between SAE and Zn anode is 75.04°, which is much lower than MAE (84.80 °) and BE (98.60 °), implying that SAE holds greater affinity with Zn anode [43].

The reversibility of Zn plating/stripping was assessed by measuring the Coulombic efficiency (CE) using the “reservoir half-cell” method [44]. As exhibited in Fig. 2a, Zn//Cu cell demonstrates the highest efficiency value with SAE (97.74%) than BE (96.66%) and MAE (97.23%). The growth of Zn nucleation has been further studied to investigate the effect of Zn deposition process on the formation of Zn dendrites. The nucleation mode can be determined by comparing the experimental dimensionless current time curve with the Scharifker model [45,46]. Fig. 2b displays the three stages of nucleation [47]. Before t_m (stage 1), it represents charge transfer and nucleation activation process. The stage 2 is considered as nucleation growth and diffusion control. After that, stage 3 is coordination of diffusion and surface reaction control process. In SAE, the cell can quickly reach the steady stage 3. According to Scharifker

model, the three-dimensional (3D) nucleation process can be divided into two types, one is instantaneous (3DI) and the other is progressive (3DP), which are described as followings:

$$\left(\frac{I}{I_m}\right)^2 = 1.9542\left(\frac{t}{t_m}\right)^{-1}\left\{1-\exp\left[-1.2564\left(\frac{t}{t_m}\right)\right]\right\}^2 \quad (1)$$

$$\left(\frac{I}{I_m}\right)^2 = \left(\frac{I}{I_m}\right)^2 = 1.2254\left(\frac{t}{t_m}\right)^{-1}\left\{1-\exp\left[-2.3367\left(\frac{t}{t_m}\right)^2\right]\right\}^2 \quad (2)$$

where the I_m is peak current response at the early stage of nucleation and t_m is the time for reaching I_m. The results exhibited in Fig. 2c indicate that the nucleation models of the three electrolytes all correspond to the instantaneous nucleation model. This suggests that the addition of additives involves reversible adsorption and does not change the nucleation mechanism in the early stage of Zn electro-crystallization. However, the

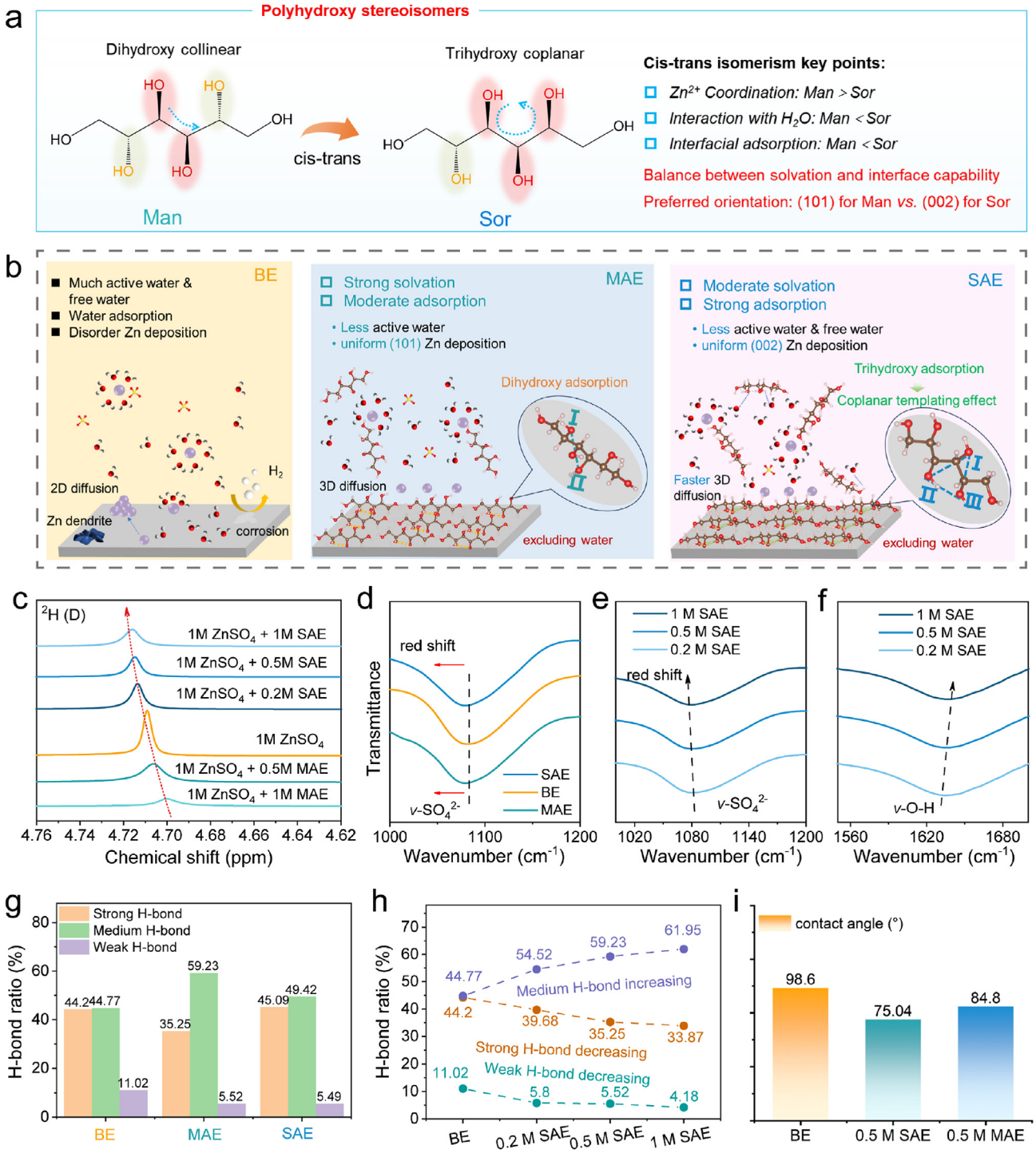

Fig. 1. (a) Molecular structure and properties of Sor and Man; (b) Schematic illustration of Zn deposition behavior and additives function in BE, MAE and SAE; (c) ^{2}H NMR spectra of electrolytes; (d–f) Fourier transform infrared spectroscopy (FTIR) of (d) three electrolytes and (e–f) SAE containing different concertation sorbitol; (g) H-bond ration in BE, MAE and SAE; (h) H-bond ration in SAE containing different concertation sorbitol; (i) Contact angles of the three electrolytes on Zn anode.

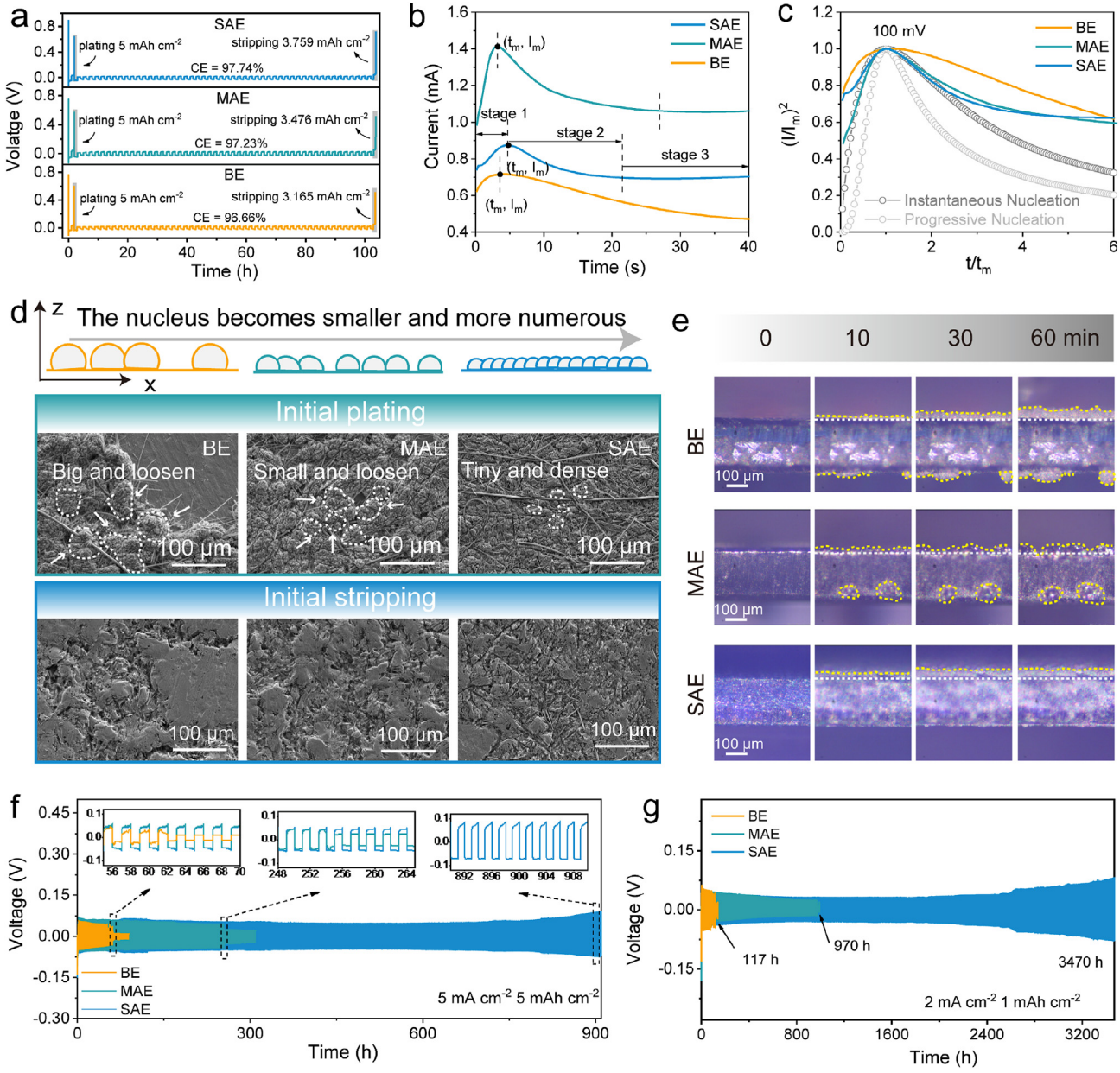

Fig. 2. (a) Coulombic efficiency tested with Zn//Cu cells; (b) *I-t* curves of symmetric cells with the three electrolytes at 100 mV; (c) Dimensionless curves $(I/I_m)^2$ vs. (t/t_m) for instantaneous and progressive nucleation; (d) Schematic diagram of nucleation and SEM images of Zn anode after initial plating/stripping in the three electrolytes; (e) In-situ optical microscope of Zn deposition process in the three electrolytes at 4 mA cm^{-2}; (f,g) Cycling performance of Zn//Zn symmetrical cells with different electrolytes at (f) 5 mA cm^{-2} and 5 mAh cm^{-2}, (g) 2 mA cm^{-2} and 1 mAh cm^{-2}.

adsorption effect of additives has an impact on the double layer, increasing the nucleation overpotential, which leads to the formation of small and large amounts of Zn deposits, inhibiting the growth of zinc dendrites. The CV tests displayed in Fig. S8 reveal the nucleation overpotential in Zn//Ti cells with three electrolytes. The value of AB represents the magnitude of nucleation overpotential. It can be clearly observed that the Zn//Ti asymmetrical batteries with MAE and SAE increase the overpotential compared to BE. The size of the nucleus can be described by the following formula:

$$r_{crit} = 2\frac{\gamma V_m}{F\eta} \tag{3}$$

in which the r_{crit} is the size of nucleus, η is the overpotential, γ represents surface energy of anode/electrolyte interface. V_m and F are molar volume of metallic Zn and Faraday constant (96485 C mol^{-1}). The larger nucleation overpotential is conductive to smaller nucleus and it shows the best effect in SAE [48].

Fig. 2d and S9 show the schematic diagram of nucleation and morphology of Zn anode after initial plating/stripping in three electrolytes. In BE, the limited number of nucleation sites with poor affinity results in relatively large and loosely formed nuclei, as well as a large area of exposure. After adding Man, although the size of the crystal nucleus is small and there are no exposed parts, it is still loose. In contrast, when Sor is introduced, the nucleation size becomes smaller and denser, which is beneficial for uniform deposition and avoids the formation of dendrites. From the high magnification SEM images (Fig. S10), the surface deposited in SAE is densest than others. In addition, the SEM images of Zn anode after initial stripping is also characterized in Fig. 2d. It can be clearly observed that Zn deposition is even with small sized pit in SAE than in BE and MAE. Furthermore, in-situ optical microscope was conducted to observe Zn deposition behavior in different electrolytes. Fig. 2e

reveals an uneven Zn plating and obvious protrusions in BE during 60 min deposition. In MAE, the Zn deposition layer is relatively uniform without large-size protrusions. By contrast, Zn plating is homogeneous and dense with SAE. These results are consistent with SEM images.

The electrochemical performance of Zn anode in these three electrolytes were investigated in symmetrical batteries. The electrolyte with 0.5 M Sor was selected as the best suit concentration (Fig. S11) and Man was also chosen at 0.5 M for the following tests. Fig. 2f compares the specific electrochemical performance in Zn//Zn symmetrical cells with different electrolytes at high current density of 5 mA cm^{-2} and a capacity of 5 mAh cm^{-2}. The cell with BE can only run for 63 h before short circuit and failure owing to Zn dendrites. With the help of Man, the cycle life of the battery can be improved to 254 h, while its function is limited. By contrast, Zn//Zn cell with SAE can cycle for fourteen times longer than that of a cell using BE, maintaining a stable voltage throughout. The cycle morphology of Zn anode at 5 mA cm^{-2} and a capacity of 5 mAh cm^{-2} was further examined. After cycling 50 h in BE, the cycled Zn anode is disorganized and covered with obvious protrusions, and the correspond surface optical image shows an uneven deposition with 27.88 μm of height (Fig. S12a). As exhibited in Fig. S12b, the cycled Zn anode in MAE is also filled with protrusions and its height is up to 19.28 μm. In comparison, the cycled Zn anode demonstrates a uniform and dendrite-free surface condition with Sor, and the surface height after cycling is only 10.62 μm (Fig. S12c). These outcomes illustrate that Man has only a minimal effect on improving surface situation. On the contrary, Sor molecules can not only induce smaller-size deposition and stripping, but also make plating process denser, reducing deposition height and relieving the problem of volume expansion. Fig. 2g also demonstrates an

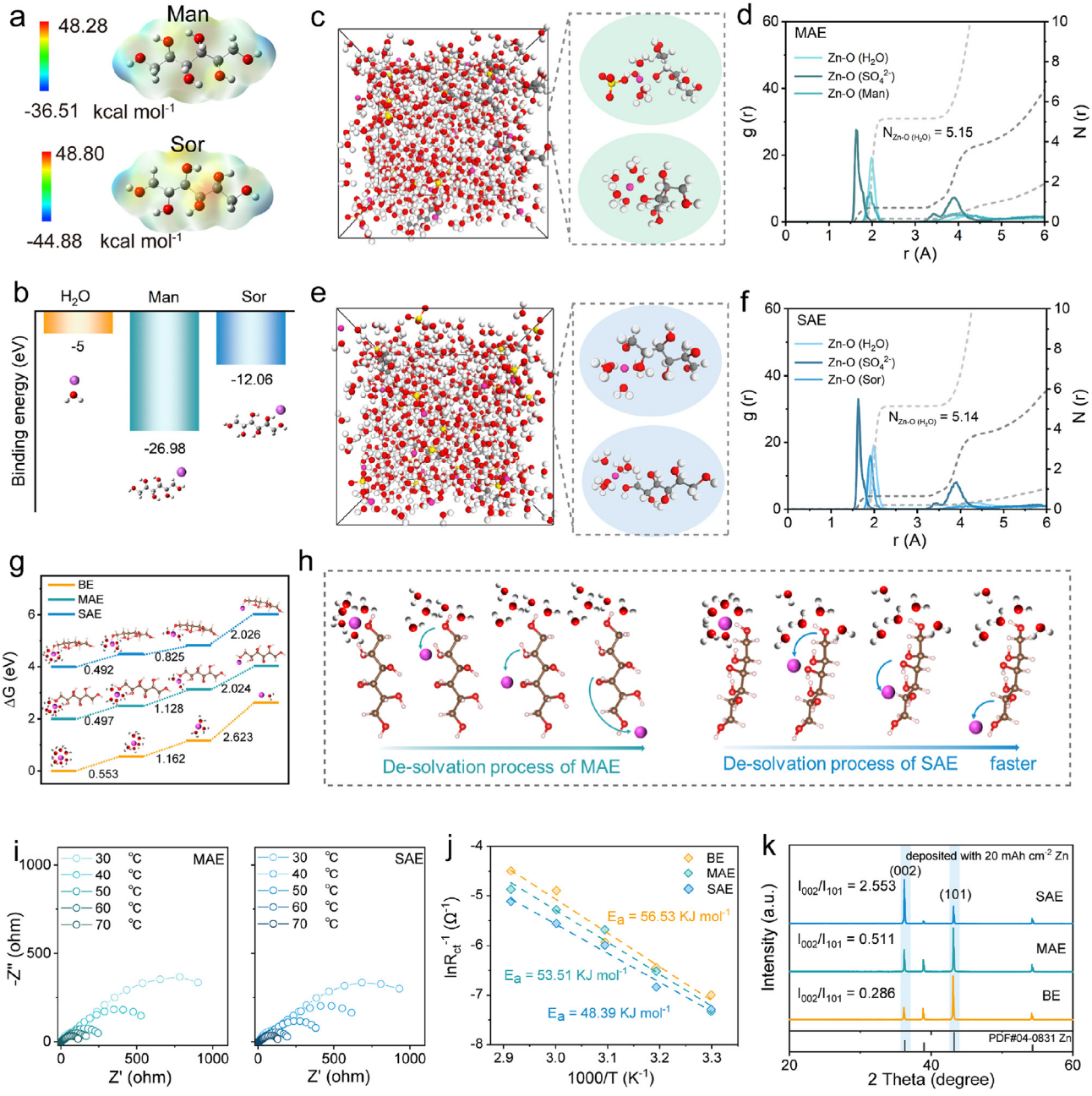

Fig. 3. (a) The electrostatic potential of Man and Sor; (b) Binding energies between H_2O, Zn^{2+}, Man and Sor; (c–f) Snapshots and RFDs of the MD simulation in (c–d) MAE and (e–f) SAE; (g) The Gibbs free energy change of de-solvation process in the three electrolytes; (h) The diagrammatic sketch of de-solvation in MAE and SAE; (i) EIS tests of Zn//Zn cells with MAE and SAE; (j) Calculated activation energies with the three electrolytes; (k) XRD patterns of deposited Zn on Ti foil in the three electrolytes.

outstanding function of SAE in symmetrical battery at 2 mA cm^{-2} and 1 mAh cm^{-2}. The battery with SAE achieves a stable cycling life of over 3470 h, substantially surpassing the performance of MAE (970 h) and BE (117 h), and demonstrating a significant advantage in stabilizing the zinc anode interface. Taking into account the performance of these symmetrical batteries, these excellent performances are superior to many representative reported symmetric Zn||Zn cells in the literature (Table S1).

These electrolytes demonstrate significant differences in both macroscopic electrolyte properties and specific battery cycling performance. The solvation ability of two additives was tested and analyzed first. Fig. 3a shows electrostatic potential (ESP) map of Man and Sor, and O atom possesses a higher electronegativity, which ensuring electrostatic interactions between Zn^{2+} ions with Man and Sor. The binding energies were calculated in Fig. 3b to identify the interaction between these species. The additives hold stronger interaction with Zn^{2+} ions than H_2O (−5 eV), which means that additives can replace H_2O position around Zn^{2+} ions, resolving in Zn^{2+} solvation structure. Moreover, the interaction between Zn^{2+} and Man (−26.98 eV) is stronger than that between Zn^{2+} and Sor (−12.06 eV), indicating strong solvation ability of Man than Sor. To theoretically investigate the Zn^{2+} solvation structure in these three electrolytes, molecular dynamics (MD) simulations were carried out. In BE, Zn^{2+} ions typically exist in the form of $(Zn(H_2O)_6)^{2+}$ or $Zn(H_2O)_5(SO_4^{2-})$, and a sharp peak appearing at ≈ 2.0 Å is recognized to the Zn-O (H_2O) (Fig. S13). As seen in Fig. 3c and d, in MAE, one Man molecule occupies the position of H_2O around Zn^{2+} ions owing to stronger interaction. The RDFs show a sharp peak at ≈ 2.0 Å which is corresponding to Zn-O (Man), proving the participation of Man in solvation structure. After adding Sor in BE, exhibited in Fig. 3e and f, one Sor molecule also replaces H_2O molecule and the sharp peak at ≈ 2.0 Å is identified as Zn-O (Sor), also confirming the function of Sor on adjusting Zn^{2+} hydration structure. The reduced H_2O molecule in solvation structure is conductive to fast de-solvation and decreasing the occurrence of HER. Fig. 3g shows the calculated Gibbs free change energies of Zn^{2+} de-solvation. The initial solvation structures are $[Zn(H_2O)_6]^{2+}$, $[Zn(H_2O)_5Man]^{2+}$ and $[Zn(H_2O)_5Sor]^{2+}$ in these three electrolytes. In the basic electrolyte, the desorption of Zn^{2+} ions is relatively challenging, as evidenced by the highest desorption energy observed. In contrast, the presence of isomeric additives significantly reduces the de-solvation energy barrier, indicating an optimized de-solvation process. Moreover, due to the relatively weak interaction between Zn^{2+} ions and Sor, and the strong binding affinity of Zn^{2+} ions to water molecules, the de-solvation energy of Zn^{2+} ions is further diminished in the presence of Sor, particularly during the removal of the first and third water molecules. This de-solvation process can be described in Fig. 3h. With the Sor, owing to stronger interaction between Zn^{2+} ion and Sor than H_2O, as well as interaction between H_2O molecule and Sor, Zn^{2+} ion can quickly remove solvated H_2O during the gradual de-solvation process. Besides, the trihydroxy group on the same side of Sor can shorten the dissolution pathway of Zn^{2+} ions and accelerate their transport. By comparison, the stronger interaction between Zn^{2+} ion and Man than H_2O improves the de-solvation process, yet, due to the strong interaction, Zn^{2+} ions require more energy to displace Man at the final stage than they do with Sor. Therefore, Zn^{2+} ions have a more significant de-solvation effect in SAE. Faster de-solvation and Zn^{2+} ion transport can also affect the deposition behavior of Zn^{2+} ions. Furthermore, EIS tests were operated with temperatures ranging from 30 °C to 70 °C to indirect compare the ability of de-solvation (Fig. 3i–j, S14). The calculated activation energies (*Ea*) are 56.53, 53.51 and 48.39 kJ mol^{-1} in BE, MAE and SAE respectively, expressing the reduced de-solvation energy barrier owing to participation of Man and Sor molecule in Zn^{2+} ion solvation structure. In addition, it has the most excellent de-solvation effect in SAE [41,49,50]. Fig. 3k presents XRD patterns of Zn plating on Ti foil with the help of fast de-solvation. The (002) plane is parallel to the substrate direction, whereas the (101) crystal plane is perpendicular to it. Growth along the (002) plane is more conducive to achieving uniform and dense deposition [51]. The peak intensity ratio of (002) to (100) is calculated after deposited with 20 mAh cm^{-2} Zn and the ratio is 0.286 (BE), 0.511 (MAE), 2.553 (SAE). This result illustrates that Man molecules have a certain effect on promoting (101) preferential growth, while Sor molecules are the most favorable for uniform and dense growth on (002) plane. Fig. S15 also exhibits the XRD pattern of Ti foil plated with 5 mAh cm^{-2} Zn in SAE, and it shows the same (002) optimal selection effect.

Afterwards, density functional theory (DFT) calculations were performed to compare the absorption behavior in different electrolytes. As shown in Fig. 4a, the adsorption energies of H_2O, Man and Sor molecules on the Zn (002) facet are −0.21 eV, −0.9 eV and −1.16 eV respectively. Both Man and Sor exhibit a greater propensity for adsorption compared to H_2O, which helps to exclude H_2O molecules near the Zn anode. Moreover, Sor with the same side trihydroxy structure has lower adsorption energy compared to dihydroxy groups on the same side structure of Man. As displayed in Fig. 4b and S16, the charge density difference of Man and Sor on Zn (002) plane Fig. 4b reveal the larger tendency of electron transfer from Sor to the surface of Zn than that of Man, indicating the stronger interactions between Sor molecule and Zn. Fig. 4b exhibits top view after adsorption Man and Sor on Zn anode. It can be clearly seen that the dihydroxy adsorption sites of Man form a straight line, while the trihydroxy adsorption sites of Sor form a triangular plane region. This coplanar triangular region can serve as a template to induce uniform distribution of charges and Zn^{2+} ions for subsequent nucleation growth. In addition, the 2D slice plan of charge density difference displayed in Fig. 4b and S17 also demonstrate the coplanar effect of triangular regions. Under the effect of triangular coplanar templating, the charge distribution on the surface of the Zn anode after adsorbing Sor is more uniform, which is more conducive to improving the number and uniformity of nucleation. Fig. 4c displays the fitting curves and corresponding EDL capacitances calculated from CV tests (Fig. S18). The value of EDL capacitance in SAE (35.28 μF cm^{-2}) is smaller than that in BE (115.96 μF cm^{-2}) and MAE (53.86 μF cm^{-2}) electrolytes, expressing the enhanced thickness of EDL owing to the adsorption of Sor molecules [52]. The water deficient EDL caused by Sor molecular adsorption is beneficial for reducing water molecule adsorption induced hydrogen evolution reactions [53].

Under this adsorption effect, the function of inhibition HER with different electrolytes was investigated. Fig. 4d is Tafel plots of Zn anode with three-electrode system at 1 mV s^{-1}. Generally speaking, a smaller corrosion current represents better corrosion resistance performance [54]. The corrosion current of Zn metal is 7.54, 4.832 and 3.674 mA cm^{-2} in BE, MAE and SAE, indicating the exceptional corrosion resistance effect with Sor [55,56]. Moreover, the linear sweep voltammetry (LSV) test displays the same results (Fig. 4e). The addition of Sor also demonstrates the best ability of suppress HER in 1 M $NaSO_4$. To characterize corrosion resistance effect, Zn foil was soaked in BE, MAE and SAE for 5 days respectively. As shown in Fig. 4f, XRD patterns of Zn metal after immersing in three electrolytes indicate that there exist obvious peaks indexed to $Zn_4SO_4(OH)_6•4H_2O$ and $Zn_4SO_4(OH)_6•H_2O$ after soaked in BE. In the meanwhile, owing to weak corrosion inhibition ability of Man, there also emerges slight peaks of by-products after immersing in MAE. By contrast, there is no evident peak after soaked in SAE, implying the optimal performance in suppressing HER with the help of Sor. Fig. 4g present SEM images and Raman spectrogram of Zn foil after immersing in different electrolytes, in which the color depth represented the intensity of sulfate (SO_4^{2-}). It can be easily observed the surface of Zn foil is uneven and filled with massive by-products, indicating the unstable state in BE. With Sor, the Zn anode demonstrates the lowest intensity of SO_4^{2-} and the least by-product. Furthermore, chronoamperometry (CA) were tested to illustrate Zn nucleation and growth behavior on Zn anode in these three electrolytes (Fig. 4h). With BE, the current density shows continuously increase within 400 s and it implies typic 2D diffusion [57]. In comparison, owing to the adsorption function of Man and Sor, Zn anode obtain a shorter 2D diffusion and stable 3D diffusion, especially in SAE. The coulombic efficiency (CE) is tested using

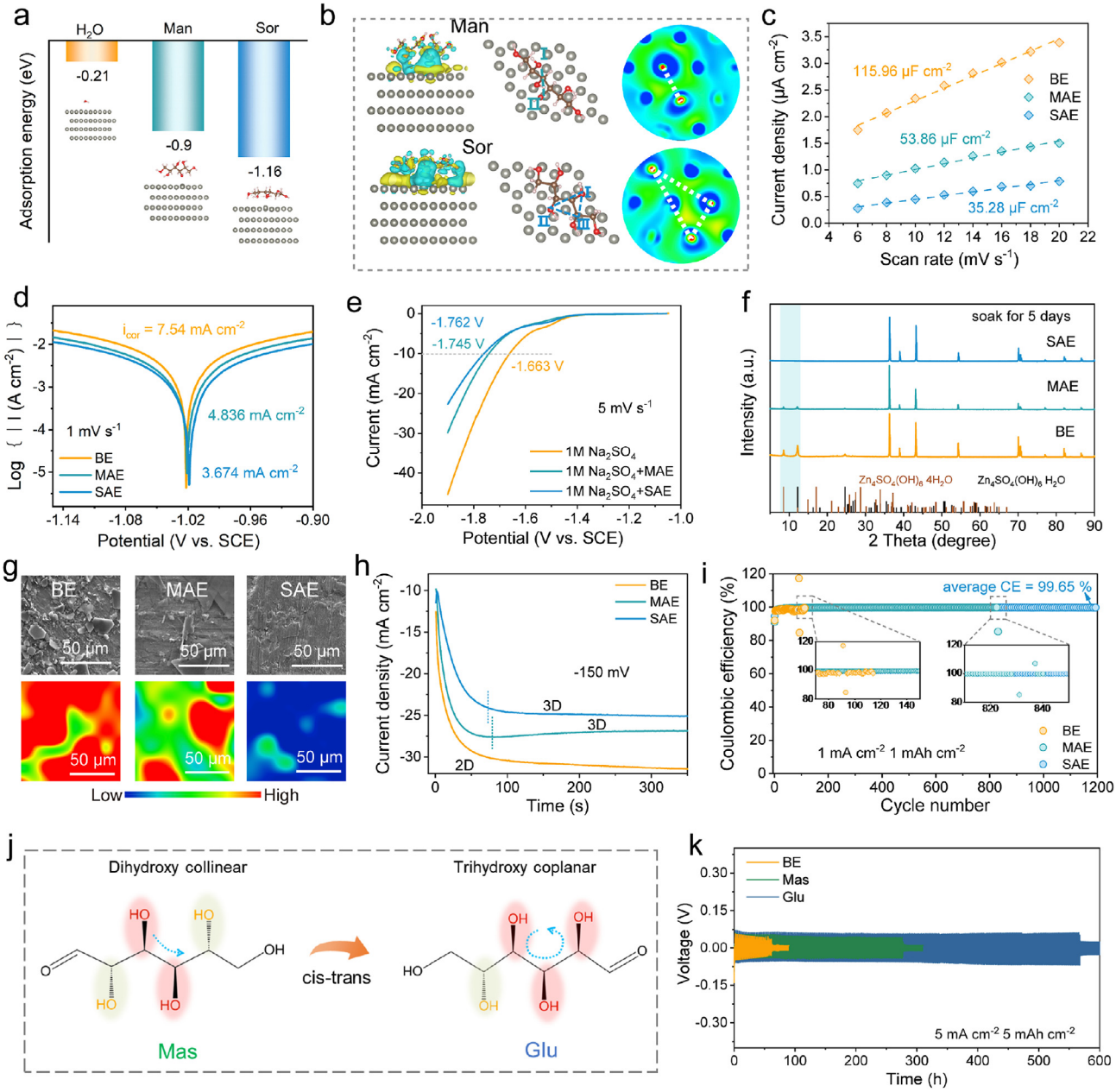

Fig. 4. (a) Adsorption energies of H_2O, Man and Sor on Zn anode; (b) The charge density and 2D slice plan of Man and Sor on Zn anode; (c) EDL measurements for Zn anode with three electrolytes; (d) Tafel plots in the three electrolytes at 1 mV s^{-1}; (e) LSV results of $NaSO_4$ with Man and Sor at 5 mV s^{-1}; (f) XRD patterns of Zn anodes after soaking in the three electrolytes; (g) SEM images and Raman spectrogram of Zn foil after immersing in BE, MAE and SAE; (h) CA curves of Zn//Zn cells with the three electrolytes at a fix potential of −150 mV; (i) Coulombic efficiencies of Zn//Cu cells with the three electrolytes; (j) Molecular Structure of Mas and Glu; (k) Cycling performance of Zn//Zn symmetrical cells with different electrolytes at 5 mA cm^{-2} and 5 mAh cm^{-2}.

Zn//Cu cells, as exhibited in Fig. 4i. The use of SAE results in an eminent reversibility of Zn plating/stripping for over 1200 cycles with an average CE of 99.65%, while the cell with BE displays a shorter cycle life only for 90 cycles. The cell with MAE exhibits an effect of extending cycle life to 828 cycles, yet short circuit. Fig. S19 are corresponding capacity-voltage curves for different cycles. It can be easily observed that the cell with SAE possesses a stable overpotential during 1200 cycles.

The same trihydroxy coplanar and dihydroxy colinear effects have also been confirmed in glucose (Glu) and mannose (Mas) with similar structures (Fig. 4j). This pair of stereoisomerisms expresses the same result as Man and Sor. As displayed in Fig. 4k, at 5 mA cm^{-2} and 5 mAh cm^{-2}, Zn//Zn cell with Glu possesses more excellent lifespan than that with Mas. This result indicates that there is a certain regularity in the effectiveness and balance selection of such effects, which provides us with a different approach in the selection of additives.

Full cells were assembled with and without Sor, using activated carbon (AC) as the cathode, to test their practical applicability. The CV curves of Zn//AC cells exhibit the rectangle-similar shape with the increase of scan rate (Fig. 5a and S20a). indicating the hybrid energy storage mechanism [58]. The EIS curves of full cells before cycling are presented in Fig. S20b and the cell with SAE holds a faster charge transfer compared in BE [59]. As demonstrates in Fig. S21, Zn//AC full cell with SAE exhibits the outstanding specific capacities and rate performance at various current density from 0.5 to 5 A g^{-1}. In addition, the Zn//AC full cell with SAE possesses an excellent cycling lifespan of 50000 cycles at 3 A g^{-1}. While, the cell with BE only run for 18000 cycles and short circuit (Fig. 5b).

Moreover, to verify the wide application of SAE, Zn//I_2 full cells were

further tested. As exhibited in Fig. 5c, the CV curves of Zn//I_2 full cells present the same redox peaks in BE and SAE, indicating that the addition of Sor does not alter the energy storage mechanism. To be more practical, the high loading of I_2 cathodes were matched with thin Zn foils (10 μm). The Zn//I_2 full cell in SAE can steadily run for nearly 230 cycles at 0.2 A g^{-1} and provide a high capacity of 176.89 mAh g^{-1} with low N/P ratio of 3.77 (Fig. 5d). However, the full cell with BE experiences short life-span and fail only after 116 cycles, which is affected by Zn dendrite and by-products induced anode failure. At 1 A g^{-1} with N/P ratio of 4.37 shown in Fig. 5e, Zn//I_2 full cell using SAE can also work for 710 cycles, demonstrating higher capacity retention of 88.21% than in BE (52.44% for 300 cycles). Fig. 5f and g are corresponding capacity-voltage curves of Zn//I_2 full cell with different electrolyte at 1 A g^{-1}. During the whole 300 cycles, the cell with BE exhibits the obvious capacity decay, while the cell with SAE shows markedly slower decay rate. These results indicate that the incorporation of Sor can not only enhance the cycling performance of symmetrical battery, but also achieve excellent performance improvement when matches with cathode in the full battery.

3. Conclusion

In summary, we exploit a pair of isomers to illustrate the impact of the balanced selection of solvation and adsorption abilities of hydroxyl rich organic small molecule additives on deposition behavior and electrochemical performance. Both Sor and Man have six hydroxyl groups, with the only difference being the hydroxyl position on the second carbon. Due to this difference, Sor with the same trihydroxy group on the same side has stronger adsorption energy and forms a coplanar templating effect, which is conducive to the preferred orientation deposition of Zn (002) and greatly improves the interface chemistry. At the same time, both molecules can participate in the solvation structure of Zn^{2+} ions, inhibiting the occurrence of hydrogen evolution corrosion. However, the strong interaction between Man and Zn^{2+} ions increase the energy required for dissolution, and the ipsilateral trihydroxy group of Sor accelerates the transport of Zn^{2+} ions, which is beneficial for the uniform deposition of Zn. Thanks to its moderate solvation ability and strong adsorption, with the help of Sor, the symmetrical battery can stably cycle for over 3470 h at 2 mA cm^{-2} and 1 mAh cm^{-2}, and the full battery also exhibits excellent electrochemical performance. Zn//AC full cell can work for 50000 cycles at 3 A g^{-1} with Sor additive. In addition, Zn//I_2 full cell under low N/P ratio of 3.77 and 4.37 can both express outstanding cycling lifespan.

4. Experimental

4.1. Preparation of electrolyte

2 M $ZnSO_4$ (BE) electrolyte was prepared by dissolving $ZnSO_4$ $7H_2O$ (AR, traditional Chinese medicine) in DI water. For electrolytes with added sorbitol (AR Aladdin) (SAE), different concentrations of sorbitol were dissolved in 2 M $ZnSO_4$ (0.1, 0.2, 0.5, 1, 2 M). For electrolytes with added mannitol (AR Aladdin) (MAE), 0.5 M mannitol was dissolved in 2 M $ZnSO_4$. For electrolytes with added glucose and mannose (AR Aladdin), 0.5 M glucose and 0.5 M mannose was dissolved in 2 M $ZnSO_4$.

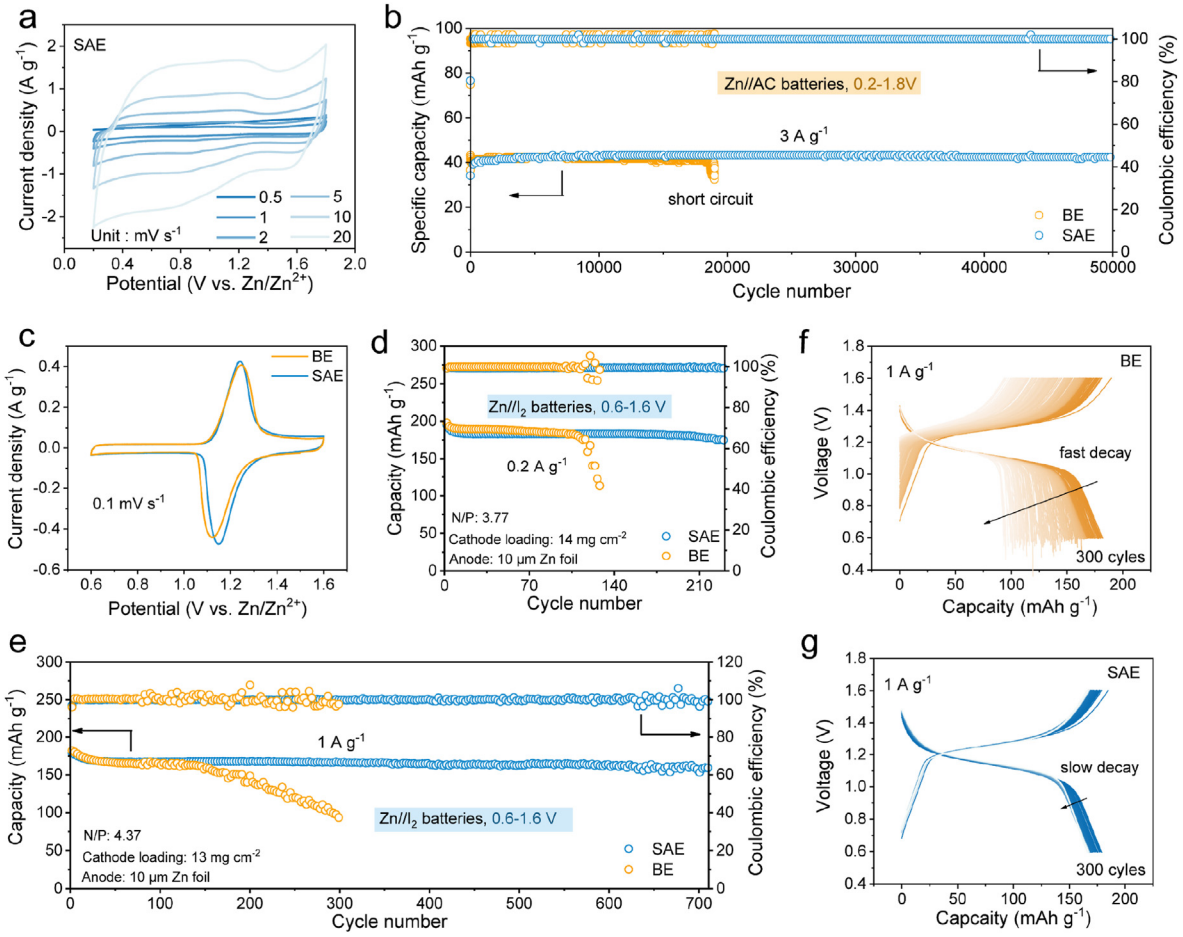

Fig. 5. (a) CV curves of Zn//AC cell at varied scan rates with SAE; (b) Long term cycling performance of Zn//AC full cell with SAE at 3 A g^{-1}; (c) CV curves of Zn//I_2 cell with Be and SAE; (d) Long term cycling performance of Zn//I_2 full cell at 0.2 A g^{-1}; (e) Long term cycling performance of Zn//I_2 full cell at 1 A g^{-1}; (f,g) Capacity-voltage curves of Zn//I_2 with (f) BE and (g) SAE at 1 A g^{-1}.

4.2. Preparation of AC cathode

Activated carbon (AC) cathode materials were prepared by mixing AC powder (Canrd), carbon black and polyvinylidene fluoride (PVDF) with a mixing weight proportion of 8:1:1 in N-methyl-2-pyrrolidone (NMP). The obtained slurry was coated on titanium (Ti) foil and the cathode materials were dried at 60 °C under a vacuum for 12 h. The AC mass loading of the electrode was about 2–2.5 mg cm^{-2}.

4.3. Preparation of I_2@AC cathode

I_2@AC powder was synthesized through a facile method. Firstly, I_2 and AC with the same quality were mixed by grinding using an agate mortar in the air at room temperature. Then, the mixed powder was sealed in a hydrothermal polytetrafluoroethylene reactor and heated at 120 °C for 6 h. After natural cooling, active carbon-enveloped I_2 (I_2@AC) powder was obtained. For I_2@AC cathode, I_2@AC powders, Ketjen black and polytetrafluoroethylene (PTFE) with a mixing weight proportion of 8:1:1 were mixed in absolute ethyl alcohol under magnetic stirring and then pressed on the titanium mesh. After drying at 60 °C for 12 h, the fabricated I_2@AC cathodes were cut into disks (12 mm) to prepare carbon cathodes for Zn-iodide (Zn//I_2) full batteries.

4.4. Electrochemical measurements

Cells were assembled in CR2032 type coins, in which the glass fiber as the separator, Zn foil (200 μm, diameter=16 mm) as anode, Cu foils, AC cathodes and I_2 cathodes (diameter=12 mm) as cathode. All galvanostatic charge and discharge tests were conducted by a Neware battery testing system. The linear sweep voltammetry (LSV) and Tafel tests were in a three-electrode system in which Zn anode was work electrode, platinum (Pt) foil was counter electrode, saturated calomel electrode (SCE) was reference electrode.

CRediT authorship contribution statement

Wen Liu: Writing – original draft, Methodology, Formal analysis, Data curation, Conceptualization. **Qiwen Zhao:** Investigation, Formal analysis. **Ruheng Jiang:** Investigation. **Xuyan Ni:** Data curation. **Tiancheng You:** Visualization. **Canglong Li:** Investigation. **Yanzi Deng:** Investigation. **Bingang Xu:** Visualization, Validation. **Yuejiao Chen:** Writing – review & editing, Resources, Funding acquisition. **Libao Chen:** Supervision, Resources.

Declaration of competing interest

The authors declare that they have no known competing financial interests or personal relationships that could have appeared to influence the work reported in this paper.

Acknowledgements

This research was financially supported by Natural Science Foundation of Hunan Province (No. 2023JJ20064) and the National Natural Science Foundation of China (No. 52377222).

Appendix A. Supplementary data

Supplementary data to this article can be found online at https://doi.org/10.1016/j.apmate.2025.100276.

References

[1] W. Liu, Q. Zhao, H. Yu, H. Wang, S. Huang, L. Zhou, W. Wei, Q. Zhang, X. Ji, Y. Chen, L. Chen, Metallic particles-induced surface reconstruction enabling highly durable zinc metal anode, Adv. Funct. Mater. 33 (38) (2023) 2302661.
[2] K. Bao, M. Wang, Y. Zheng, P. Wang, L. Yang, Y. Jin, H. Wu, B. Sun, Construction of low dielectric aqueous electrolyte with ethanol for highly stable Zn anode, Nano Energy 120 (2024) 109089.
[3] Z. Ma, Z. Xie, J. Liu, J. Vatamanu, L. Xing, W. Li, Distinct roles: Co-solvent and additive synergy for expansive electrochemical range and low-temperature aqueous batteries, Energy Storage Mater. 66 (2024) 103203.
[4] H. Tang, N. Hu, L. Ma, H. Weng, D. Huang, J. Zhu, H. Yang, Z. Chen, X. Yin, J. Xu, H. He, Interfacial dual-modulation via cationic electrostatic shielding and anionic preferential adsorption toward planar and reversible zinc electrodeposition, Adv. Funct. Mater. 34 (2024) 2402484.
[5] Z. Wang, L. Yang, C. Xu, J. Cheng, J. Zhao, Q. Huang, C. Yang, Advances in reactive co-precipitation technology for preparing high-performance cathodes, Green Carbon 1 (2) (2023) 193–209.
[6] Y. Zhong, C. Cao, L. Zhao, M.O. Tadé, Z. Shao, Optimization of two-dimensional solid-state electrolyte–anode interface by integrating zinc into composite anode with dual-conductive phases, Green Carbon 2 (1) (2024) 94–100.
[7] J. Hao, L. Yuan, Y. Zhu, X. Bai, C. Ye, Y. Jiao, S. Qiao, Low-cost and non-flammable eutectic electrolytes for advanced Zn-I_2 batteries, Angew. Chem. Int. Ed. 62 (39) (2023) e202310284.
[8] P. Li, J. Zhang, Y. Chen, L. Zhang, Z. Zhao, Z. Peng, Interfacial H_2O structure matters: realizing stable zinc anodes with trace acesulfame-K in aqueous electrolyte, Adv. Funct. Mater. 34 (27) (2024) 2316605.
[9] W. Liu, Y. Chen, Y. Wang, Q. Zhao, L. Chen, W. Wei, J. Ma, Influence of anion substitution on 3D-architectured Ni-Co-A (A=H, O, P) as efficient cathode materials towards rechargeable Zn-based battery, Energy Storage Mater. 37 (2021) 336–344.
[10] M. Wang, Y. Meng, K. Li, T. Ahmad, N. Chen, Y. Xu, J. Sun, M. Chuai, X. Zheng, Y. Yuan, C. Shen, Z. Zhang, W. Chen, Toward dendrite-free and anti-corrosion Zn anodes by regulating a bismuth-based energizer, eScience 2 (5) (2022) 509–517.
[11] Z. Feng, Y. Zhang, Z. Gao, D. Hu, H. Jiang, T. Hu, C. Meng, Y. Zhang, Construction interlayer structure of hydrated vanadium oxides with tunable P-band center of oxygen towards enhanced aqueous Zn-ion batteries, Adv. Powder Mater. 3 (2) (2024) 100167.
[12] F. Jing, C. Lv, L. Xu, Y. Shang, J. Pei, P. Song, Y. Wang, G. Chen, C. Yan, An amorphous manganese iron oxide hollow nanocube cathode for aqueous zinc ion batteries, J. Energy Chem. 87 (2023) 314–321.
[13] F. Jing, Y. Liu, Y. Shang, C. Lv, L. Xu, J. Pei, J. Liu, G. Chen, C. Yan, Dual ions intercalation drives high-performance aqueous Zn-ion storage on birnessite-type manganese oxides cathode, Energy Storage Mater. 49 (2022) 164–171.
[14] W. Cheng, M. Zhao, Y. Lai, X. Wang, H. Liu, P. Xiao, G. Mo, B. Liu, Y. Liu, Recent advances in battery characterization using in situ XAFS, SAXS, XRD, and their combining techniques: from single scale to multiscale structure detection, Exploration 4 (1) (2024) 20230056.
[15] C. Wang, Y. Yang, S. Zhang, Z. Yang, Y. Song, Z. Tang, T. Sang, F. Wan, S. Sun, W. Chen, The impact of surface functional groups on mxene anode protective layer in aqueous zinc-ion batteries: understanding the mechanism, J. Energy Storage 94 (2024) 112360.
[16] C. Wang, Y. Li, S. Zhang, T. Sang, Y. Lei, R. Liu, F. Wan, Y. Chen, W. Chen, Y. Zheng, S. Sun, Organic cation-supported layered vanadate cathode for high-performance aqueous zinc-ion batteries, Carbon Energy e647 (2024), https://doi.org/10.1002/cey2.647.
[17] Q. Zhao, W. Liu, X. Ni, H. Yu, C. Zhang, B. Wang, L. Jiang, H. He, Y. Chen, L. Chen, Steering interfacial renovation with highly electronegative cl modulated trinity effect for exceptional durable zinc anode, Adv. Funct. Mater. 34 (41) (2024) 2404219.
[18] Z. Cai, J. Wang, Y. Sun, Anode corrosion in aqueous Zn metal batteries, eScience 3 (1) (2023) 100093.
[19] X. Cao, W. Xu, D. Zheng, F. Wang, Y. Wang, X. Shi, X. Lu, Weak solvation effect induced optimal interfacial chemistry enables highly durable Zn anodes for aqueous Zn-ion batteries, Angew. Chem. Int. Ed. 63 (6) (2024) e202317302.
[20] X. Shi, J. Xie, J. Wang, S. Xie, Z. Yang, X. Lu, A weakly solvating electrolyte towards practical rechargeable aqueous zinc-ion batteries, Nat. Commun. 15 (1) (2024) 302.
[21] H. Huang, Z. Zhao, P. Li, H. Zhang, G. Li, Optimizing electrolyte systems for stable and low-temperature zinc-ion batteries via efficient coordinator, J. Power Sources 602 (2024) 234340.
[22] W. Zhong, Z. Shen, J. Mao, S. Zhang, H. Cheng, Y. Kim, Y. Lu, Mitigating cathodic dissolution through interfacial water masking to enhance the longevity of aqueous zinc–ion batteries, Energy Environ. Sci. 17 (5) (2024) 2059–2068.
[23] H. Cao, X. Zhang, B. Xie, X. Huang, F. Xie, Y. Huo, Q. Zheng, R. Zhao, Q. Hu, L. Kang, S. Liu, D. Lin, Unraveling the solvation structure and electrolyte interface through carbonyl chemistry for durable and dendrite-free Zn anode, Adv. Funct. Mater. 33 (46) (2023) 2305683.
[24] Y. Bai, D. Deng, J. Wang, Y. Wang, Y. Chen, H. Zheng, M. Liu, X. Zheng, J. Jiang, H. Zheng, M. Yi, W. Li, G. Fang, D. Wang, Y. Lei, Inhibited passivation by bioinspired cell membrane Zn interface for Zn–air batteries with extended temperature adaptability, Adv. Mater. 36 (40) (2024) 2411404.
[25] Q. Wang, Q. Feng, Y. Lei, S. Tang, L. Xu, Y. Xiong, G. Fang, Y. Wang, P. Yang, J. Liu, W. Liu, X. Xiong, Quasi-solid-state Zn-air batteries with an atomically dispersed cobalt electrocatalyst and organohydrogel electrolyte, Nat. Commun. 13 (1) (2022) 3689.
[26] H. Yu, D. Chen, L. Zhang, S. Huang, L. Zhou, G. Kuang, W. Wei, L. Chen, Y. Chen, Electrolyte engineering for optimizing anode/electrolyte interface towards superior aqueous zinc-ion batteries: a review, Trans. Nonferrous Met. Soc. China 34 (10) (2024) 3118–3150.
[27] H. Ren, S. Li, B. Wang, Y. Gong, H. Zhang, J. Wang, Q. Lv, D. Wang, H. Liu, S. Dou, Mapping the design of electrolyte additive for stabilizing zinc anode in aqueous zinc ion batteries, Energy Storage Mater. 68 (2024) 103364.

[28] Y. Song, W. Lu, H. Yang, C. Wu, W. Wei, G. Kuang, Y. Chen, L. Chen, X. Ouyang, Ionic-cellulose-adhesive modulated aqueous electrolyte enables water-poor and stable anion-derived electrolyte interphase for durable and dendrite-free zinc metal batteries, Nano Energy 120 (2024) 109094.
[29] S. Xu, J. Huang, G. Wang, Y. Dou, D. Yuan, L. Lin, K. Qin, K. Wu, H.K. Liu, S. Dou, C. Wu, Electrolyte and additive engineering for Zn anode interfacial regulation in aqueous zinc batteries, Small Methods 8 (6) (2024) 2300268.
[30] K. Xie, K. Ren, Q. Wang, Y. Lin, F. Ma, C. Sun, Y. Li, X. Zhao, C. Lai, In situ construction of zinc-rich polymeric solid–electrolyte interface for high-performance zinc anode, eScience 3 (4) (2023) 100153.
[31] Q. Wang, S. Tang, Z. Wang, J. Wu, Y. Bai, Y. Xiong, P. Yang, Y. Wang, Y. Tan, W. Liu, X. Xiong, Y. Lei, Electrolyte tuned robust interface toward fast-charging Zn–air battery with atomic Mo site catalyst, Adv. Funct. Mater. 33 (47) (2023) 2307390.
[32] K. Roy, A. Rana, T.K. Ghosh, J.N. Heil, S. Roy, K.J. Vannoy, B.M. Tackett, M. Chen, J.E. Dick, How solvation energetics dampen the hydrogen evolution reaction to maximize zinc anode stability, Adv. Energy Mater. 14 (15) (2024) 2303998.
[33] X. Wu, Y. Xia, S. Chen, Z. Luo, X. Zhang, Y. Lu, H. Pan, B.B. Xu, M. Yan, Y. Jiang, Transient zwitterions dynamics empowered adaptive interface for ultra-stable Zn plating/stripping, Small 20 (8) (2024) 2306739.
[34] M.J. Sottomayor, F. Silva, Adsorption of mannitol and sorbitol on gold(111), J. Electroanal. Chem. 376 (1) (1994) 59–64.
[35] M. Siniti, S. Jabrane, J.M. Létoffé, Study of the respective binary phase diagrams of sorbitol with mannitol, maltitol and water, Thermochim. Acta 325 (2) (1999) 171–180.
[36] J.R. Grigera, Conformation of polyols in water. Molecular-dynamics simulation of mannitol and sorbitol, J. Chem. Soc., Faraday Trans. 84 (8) (1988) 2603–2608.
[37] Y. Hu, J. Fu, H. Hu, D. Ho, H. Hu, Differentiating contribution to desolvation ability from molecular structure and composition for screening highly-effective additives to boost reversibility of zinc metal anode, Energy Storage Mater. 55 (2023) 669–679.
[38] M. Qiu, P. Sun, G. Cui, W. Mai, Chaotropic polymer additive with ion transport tunnel enable dendrite-free zinc battery, ACS Appl. Mater. Interfaces 14 (36) (2022) 40951–40958.
[39] D. Xu, X. Ren, H. Li, Y. Zhou, S. Chai, Y. Chen, H. Li, L. Bai, Z. Chang, A. Pan, H. Zhou, Chelating additive regulating Zn-ion solvation chemistry for highly efficient aqueous zinc-metal battery, Angew. Chem. Int. Ed. 63 (21) (2024) e202402833.
[40] T. Xiao, J. Yang, B. Zhang, J. Wu, J. Li, W. Mai, H.J. Fan, All-round ionic liquids for shuttle-free zinc-iodine battery, Angew. Chem. Int. Ed. 63 (8) (2024) e202318470.
[41] F. Tan, X. Cai, W. Yan, Q. Wang, J. Zhao, W. Zhang, Natural honey helps stabilize zinc anode for dendrite-free aqueous zinc ion batteries, Energy Storage Mater. 67 (2024) 103273.
[42] Y. Su, L. Xu, Y. Sun, W. Guo, X. Yang, Y. Zou, M. Ding, Q. Zhang, C. Qiao, S. Dou, T. Cheng, J. Sun, A holistic additive protocol steers dendrite-free Zn(101) orientational electrodeposition, Small 20 (11) (2024) 2308209.
[43] J. Zhou, H. Yu, P. Qing, D. Chen, S. Huang, Y. Jin, H. He, G. Zhou, Z. Xie, Y. Chen, Interfacial double-coordination effect reconstructing anode/electrolyte interface for long-term and highly reversible Zn metal anodes, J. Colloid Interface Sci. 678 (2025) 772–782.
[44] L. Liu, H. Lu, C. Han, X. Chen, S. Liu, J. Zhang, X. Chen, X. Wang, R. Wang, J. Xu, H.K. Liu, S.X. Dou, W. Li, Salt anion amphiphilicity-activated electrolyte cosolvent selection strategy toward durable Zn metal anode, ACS Nano 17 (22) (2023) 23065–23078.
[45] S. Chen, J. Chen, X. Liao, Y. Li, W. Wang, R. Huang, T. Zhao, S. Yan, Z. Yan, F. Cheng, H. Wang, Enabling low-temperature and high-rate Zn metal batteries by activating Zn nucleation with single-atomic sites, ACS Energy Lett. 7 (11) (2022) 4028–4035.
[46] Z. Shen, J. Mao, G. Yu, W. Zhang, S. Mao, W. Zhong, H. Cheng, J. Guo, J. Zhang, Y. Lu, Electrocrystallization regulation enabled stacked hexagonal platelet growth toward highly reversible zinc anodes, Angew. Chem. Int. Ed. 62 (11) (2023) e202218452.
[47] M. Li, C. Xi, X. Wang, L. Li, Y. Xiao, Y. Chao, X. Zheng, Z. Liu, Y. Yu, C. Yang, Spontaneous desaturation of the solvation sheath for high-performance anti-freezing zinc-ion gel-electrolyte, Small 19 (35) (2023) 2301569.
[48] J. Wu, B. Song, Z. Ge, X. Xiao, W. Deng, G. Zou, H. Hou, X. Ji, Bifunctional electrolyte additive for stable Zn anode: reconstructing solvated structure and guiding oriented growth of Zn, Energy Storage Mater. 63 (2023) 103000.
[49] H. Qin, W. Kuang, N. Hu, X. Zhong, D. Huang, F. Shen, Z. Wei, Y. Huang, J. Xu, H. He, Building metal-molecule interface towards stable and reversible Zn metal anodes for aqueous rechargeable zinc batteries, Adv. Funct. Mater. 32 (47) (2022) 2206695.
[50] L. Yuan, J. Hao, B. Johannessen, C. Ye, F. Yang, C. Wu, S. Dou, H. Liu, S. Qiao, Hybrid working mechanism enables highly reversible Zn electrodes, eScience 3 (2) (2023) 100096.
[51] S. Wu, Z. Hu, P. He, L. Ren, J. Huang, J. Luo, Crystallographic engineering of Zn anodes for aqueous batteries, eScience 3 (3) (2023) 100120.
[52] K. Qiu, G. Ma, Y. Wang, M. Liu, M. Zhang, X. Li, X. Qu, W. Yuan, X. Nie, N. Zhang, Highly compact zinc metal anode and wide-temperature aqueous electrolyte enabled by acetamide additives for deep cycling Zn batteries, Adv. Funct. Mater. 34 (18) (2024) 2313358.
[53] X. Ma, H. Yu, C. Yan, Q. Chen, Z. Wang, Y. Chen, G. Chen, C. Lv, Nitroxyl radical triggered the construction of a molecular protective layer for achieving durable Zn metal anodes, J. Colloid Interface Sci. 664 (2024) 539–548.
[54] F. Jing, L. Xu, Y. Shang, G. Chen, C. Lv, C. Yan, Interface engineering enabled by sodium dodecyl sulfonate surfactant for stable Zn metal batteries, J. Colloid Interface Sci. 669 (2024) 984–991.
[55] C. Ma, X. Wang, W. Lu, K. Yang, N. Chen, H. Jiang, C. Wang, H. Yue, D. Zhang, F. Du, Dual-parasitic effect enables highly reversible Zn metal anode for ultralong 25,000 cycles aqueous zinc-ion batteries, Nano Lett. 24 (13) (2024) 4020–4028.
[56] M. Fu, Q. Zhao, K. Long, Q. Li, G. Kuang, L. Zhou, W. Wei, X. Ji, L. Chen, Y. Chen, Global "interface-space" dual-modulation by functional supramolecules organic frameworks on aqueous zinc-ion batteries, Adv. Funct. Mater. 34 (10) (2024) 2311680.
[57] Q. Li, H. Wang, H. Yu, M. Fu, W. Liu, Q. Zhao, S. Huang, L. Zhou, W. Wei, X. Ji, Y. Chen, L. Chen, Engineering an ultrathin and hydrophobic composite zinc anode with 24 μm thickness for high-performance Zn batteries, Adv. Funct. Mater. 33 (40) (2023) 2303466.
[58] M. Qiu, P. Sun, A. Qin, G. Cui, W. Mai, Metal-coordination chemistry guiding preferred crystallographic orientation for reversible zinc anode, Energy Storage Mater. 49 (2022) 463–470.
[59] Q. Zhao, W. Liu, Y. Chen, L. Chen, Ultra-stable Zn metal batteries with dendrite-free Cu-Sn alloy induced high-quality composite Zn mesh, Chem. Eng. J. 450 (2022) 137979.

Wen Liu received his Master degree in materials science and engineering from the Central South University (2021). He is now a Ph.D. candidate in Central South University. His current research interests include advanced energy storage devices, especially for aqueous zinc batteries and capacitors.

Yuejiao Chen is an associate professor working for the State Key Laboratory of Powder Metallurgy, Central South University, China. She received her Ph.D. degree from Hunan University in 2015 and then engaged in postdoctoral research at The Hong Kong Polytechnic University (2016–2018). Her research interests focus on high-performance batteries such as zinc-/lithium-ion batteries and flexible energy devices.

Libao Chen received his Bachelor degree and Master degree from Central South University in 2001 and 2004, respectively, and a Ph.D. degree from the Shanghai Institute of Microsystem and Information Technology, Chinese Academy of Sciences in 2007. He is now a professor in the State Key Laboratory of Power Metallurgy at Central South University. His main research interest is focused on the high-performance energy storage materials and devices, including Li alloy anode, Zinc anode, lithium-ion batteries, and lithium–sulfur batteries.